Stable and efficient nanofilm pure evaporation on nanopillar surfaces

Jin Huan Pu[a], Si Kun Wang[a], Jie Sun[b*], Wen Wang[a] and Hua Sheng Wang[a]

[a]*School of Engineering and Materials Science, Queen Mary University of London, London E1 4NS, UK*

[b]*School of Chemical Engineering and Technology, Xi'an Jiaotong University, Xi'an, Shaanxi 710049, China*

ABSTARCT: Molecular dynamics simulations were conducted to systematically investigate how to maintain and enhance nanofilm pure evaporation on nanopillar surfaces. Firstly, the dynamics of the evaporation meniscus, and the onset and evolution of nanobubbles on nanopillar surfaces were characterized. The meniscus can be pinned at the top surface of the nanopillars during evaporation for perfectly wetting fluid. The curvature of the meniscus close to nanopillars varies dramatically. Nanobubbles do not originate from the solid surface, where there is an ultrathin non-evaporation film due to strong solid-fluid interaction, but originate and evolve from the corner of nanopillars, where there is a quick increase in potential energy of fluid. Secondly, according to parametric study, smaller pitch between nanopillars (P) and larger diameter of nanopillar (D) are found to enhance evaporation but also raise the possibility of boiling, whereas smaller height of nanopillar (H) is found to enhance evaporation and suppress boiling. Finally, it is revealed that the nanofilm thickness should be maintained beyond a threshold, which is 20 Å in this work, to avoid the suppression effect of disjoining pressure on evaporation. Moreover, it is revealed that whether the evaporative heat transfer is enhanced on the nanopillar surface compared with the smooth surface is also affected by the nanofilm thickness. The value of nanofilm thickness should be determined by the competition between the suppression effect on evaporation due to the decrease in the volume of supplied fluid and the existence of capillary pressure and the enhancement effect on evaporation due to the

increase in the heating area. Our work serves as the guidelines to achieve stable and efficient nanofilm pure evaporative heat transfer on nanopillar surfaces.

INTRODUCTION

Due to utilizing high latent heat of vaporization, evaporation has received particular interest in the last few decades [1]-[9], e.g., cooling electronics and photonics devices [10][11] and solar vapor generation [12]. Particularly, capillary-fed, thin-film evaporation device using wicks has drawn increasing attention because of its passively fluid replenishment ability and efficient heat transfer performance.

Many efforts have been driven to understand the governing physics and improve device performance [13]-[25]. Ravi et al. [14] fabricated different micropillar array wicks to assess the accuracy of various existing models for permeability and capillary pressure. An overall model for predicting the liquid mass flow rate was developed by combining two most accurate models. Adera et al. [16] carried out systematic experiments to characterize the capillary-fed thin-film evaporation from micropillar wicks and developed a semi-analytical model to determine the capillary-limited dry-out heat flux and wall temperature with ±20% accuracy. Antao et al. [20] used a transient laser interferometry technique to investigate the evolution of the liquid meniscus in micropillar arrays during evaporation. They found that there are two stages during the dynamics evaporation and the receding contact angle is independent of the structure geometry and the rate of evaporation. Zhang et al. [24] used a custom micro-Raman spectroscopy platform to achieve the measurement of local thin film temperature and mapping the overall temperature distribution on the microstructure surface at different heat fluxes.

However, in prior studies, the dynamics of liquid meniscus has not been accurately measured due to the technique limitation, especially the evolution of the liquid meniscus near nanopillars. Additionally, most investigation had been carried out directly based on pure evaporation like above mentions. Although some works [26]-[28] observed the existence of boiling in those capillary-fed evaporators, the onset and evolution of nanobubbles in the wicks and how to avoid boiling have not been clearly characterized. To design a reliable capillary-fed evaporator, pure

evaporation in the absence of boiling is preferred due to its stable nature compared with the chaotic boiling process and the boiling limit [6]. So, the understanding how to maintain stable evaporation is necessary. Finally, as we know the film thickness from cell to cell in capillary-fed evaporator is different due to the pressure gradient across the substrate [19][25], but the effect of film thickness on evaporation in nanopillars remains limited in previous numerical and experimental studies and its role in the maintenance and enhancement of evaporation needs more investigation.

Molecular dynamics (MD) method is a powerful tool to elucidate phenomena from molecular level and provide fundamental understanding not accessible by experiments or CFD simulations. Therefore, in this work MD method is employed to investigate how to maintain and enhance stable and efficient nanofilm evaporation without boiling. Moreover, to enrich the understanding of evaporation process, the dynamics of evaporation meniscus is also characterized from molecular insight. The onset and evolution of nanobubbles on nanopillar surfaces is captured and elucidated on the basis of energy analysis. Our work provides useful guidelines to understand and optimize the heat transfer performance of nanopillar wicks.

COMPUTATIONAL METHODS

In this work, nanofilm evaporation on nanopillar surfaces was investigated using MD method. All the simulations are conducted using LAMMPS (Large-scale/molecular massively parallel simulator) software package [29]. A schematic of nanopillar array is depicted in Fig. 1(a). The geometry parameters of a unit cell are noted in Fig. 1(b). H and D are the height and diameter of the nanopillar, and P is the pitch between the pillars. δ is defined as the nanofilm thickness. Nanofilm evaporation on the surfaces of a unit cell is simulated and the MD model is shown in Fig. 1(d). Correspondingly, nanofilm evaporation on a smooth surface, is also simulated (see Fig. 1(e)). The overall size of all simulation boxes measures $l_x \times l_y \times l_z = P \times P \times 92\ a$, where a is the lattice constant ($a = 0.392$ nm). The nanopillars and solid substrate are constructed by Pt-

4

like atoms arranged in the face-centered cubic (FCC) lattice, and the length of the unit cell is a. The solid substrate consists of three layers of Pt-like atoms and one extra layer of Pt-like atoms is fixed at the lowermost end to serve as a frame. In the x and y-directions, periodic boundary conditions are used, while in the z-direction, the fixed boundary condition is employed, and the reflection boundary condition is also applied at the uppermost end. The embedded-atom method (EAM) potential is applied to model the interactions among solid atoms. The total energy of an atom i is described by:

$$\varphi_i\left(r_{ij}\right)=F_\alpha\left(\sum_{j\neq i}\rho_\beta\left(r_{ij}\right)\right)+\frac{1}{2}\sum_{j\neq i}\phi_{\alpha\beta}\left(r_{ij}\right) \tag{1}$$

where F is the embedding energy, and it is the energy to embed atom i into the background electron density. α and β are the element types of atoms i and j. ρ is the host electron density at atom i due to the remaining atoms of the system. φ is the pair potential interaction. The 12-6 Lennard-Jones (LJ) potential is employed to model the fluid-fluid atoms interaction and fluid-solid atoms interaction:

$$\varphi(r)=4\varepsilon\left[\left(\frac{\sigma}{r}\right)^{12}-\left(\frac{\sigma}{r}\right)^{6}\right] \tag{2}$$

where r is the intermolecular separation, ε and σ are the energy and length characteristic parameters, respectively. The potential function is truncated at the cut-off radius $r_c = 3.5$ σ_{ff}, beyond which atom interactions are ignored. For the interaction between fluid atoms, $\varepsilon_{ff} = 0.0104$ eV and $\sigma_{ff} = 3.40$ Å. For the interaction between fluid-solid atoms, $\varepsilon_{fs} = 2\varepsilon_{ff}$ and $\sigma_{fs} = 0.91\sigma_{ff}$, which guarantees a strong surface wettability [30][31] and benefits mass and heat transfer.

All the simulations are performed with a time step of 5 fs. The system is first equilibrated at $T = 100$ K for 7 ns using a Berendsen thermostat. Afterwards, fluid properties at equilibrium state

were calculated. The NEMD (non-equilibrium molecular dynamics) simulation is initiated by increasing the solid temperature. Simultaneously, the thermostat added on fluid molecules is removed and only NVE ensemble is employed. Additionally, to save simulation cost and eliminate the effect of pressure increase due to evaporation, the vapor atoms propagating into a region with thickness of $15a$ at the uppermost end are removed. In the present work, a parametric study of achieving stable and efficient evaporation without boiling was conducted by varying P, D, and H between 48-80, 8-32, and 24-50 a ($a = 0.392$ nm), respectively. Simulation cases are conveniently denoted by their typical geometry parameters. For example, the simulation case with $P = 48a$, $D = 16a$, and $H = 36a$ is denoted as $P48D16H36$.
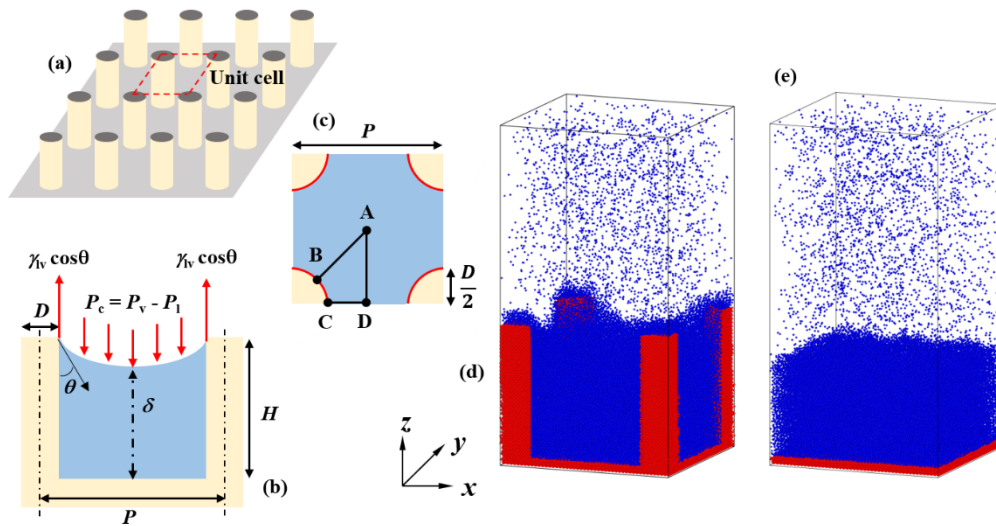

Fig. 1. (a) Schematic of a typical nanopillar array. (b) Front view of a unit cell in a nanopillar array, where P, D and H represent the pitch between two pillars, the diameter and height of the pillar, respectively. θ and δ are the contact angle and nanofilm thickness. Force analysis on the meniscus in the vertical direction is also depicted, where γ_{lv} is liquid-vapor surface tension, and P_c, P_v, and P_l are capillary pressure, vapor pressure and liquid pressure, respectively. (c) Top view of a unit cell in a nanopillar array. The red lines represent the triple-phase contact line of the meniscus around nanopillars. (d) Schematic of the computational model for a unit cell in a nanopillar array. Solid atoms are in red, and fluid molecules are in blue. (e) Schematic of the computational model for nanofilm evaporation on a smooth surface.

RESULTS AND DISCUSSION

Capillary Pressure

After the simulation system evolves to equilibrium state, a meniscus is formed due to the existence of surface tension. Correspondingly, there is a pressure difference between the liquid and vapor side of the meniscus. This pressure difference is named as capillary pressure (P_c). For capillary-fed evaporator, accurately quantifying capillary pressure is quite important when we try to design or improve its performance. In MD simulation, the capillary pressure can be directly determined from the difference between vapor pressure (P_v) and liquid pressure (P_l): $P_c = P_v - P_l$. The MD results (P_c_MD) are shown in Fig. 2. As can be seen, increasing P leads to the decrease in P_c when D and H are fixed. For fixed P and H, P_c can be increased by increasing D. Additionally, the capillary pressure in a nanopillar array can also be obtained by a force balance method [20]. In the equilibrium stage, there shows a steady meniscus, on which the downward force due to capillary pressure (F_c), namely the force due to the pressure difference between liquid and vapor sides of the meniscus, is opposed by the upward force due to the surface tension (F_γ) on the circumference of the nanopillars. Considering a unit cell (see Fig. 1b and Fig.1c),

$$F_c = P_c A_{\text{vertical}} = P_c \left(P^2 - \frac{\pi D^2}{4} \right) \tag{3}$$

$$F_\gamma = \pi D \gamma_{\text{lv}} \cos \theta \tag{4}$$

where A_{vertical} is the vertical projected area of the meniscus, γ_{lv} is the liquid-vapor surface tension and θ is the contact angle. At mechanical balance, $F_c = F_\gamma$, hence

$$P_c = \frac{4\gamma_{\text{lv}} \cos \theta}{D \left[\frac{4}{\pi} \left(\frac{P}{D} \right)^2 - 1 \right]} . \tag{5}$$

To obtain γ_{lv}, an EMD (equilibrium molecular dynamics) system is simulated (see Sec. 1 in supporting information). For $T = 100$ K, $\gamma_{lv} = 8.964$ mN·m^{-1} and $\rho_{sat} = 1285$ kg·m^{-3}, where ρ_{sat} is saturated fluid density. To obtain θ, the liquid-vapor interface location, where the fluid density is half of the bulk liquid density, is extracted and these data are fitted to a two-term exponential function. Considering the non-axisymmetric nature of the meniscus around a nanopillar, θ in Eq. 5 is calculated by the average of θ in CD direction and AB direction (see Fig. 1c). The capillary pressure determined from analytical solution (P_c_Eq.5) is compared with that from MD (P_c_MD) in Fig. 2. As can be seen, they are in good agreement.
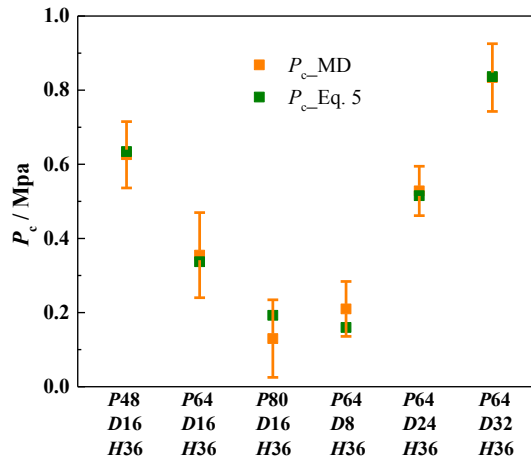
Fig. 2 Comparison of capillary pressure determined from MD simulation (P_c_MD) and from analytical solution (P_c_Eq.5).

Dynamics of Evaporation Meniscus

When the solid temperature is increased, evaporation appears, and the meniscus develops. To examine the dynamic behavior of the evaporation meniscus, the liquid-vapor interface, where $\rho = 0.009$ Å^{-3}, is extracted from the density contour of fluid. To identify the location of the vapor-liquid interface, the number of fluid neighbors of a fluid molecule within a certain distance ($1.5\sigma_{ff}$), named as the coordination number (CN), is collected for every fluid molecule. Afterwards the normalized histogram of the coordination number per fluid molecule during evaporation is analyzed. Fig. 3 presents a typical distribution. It is seen that the low faction is

always located between CN = 2 to 4. To further identify liquid and vapor molecules during evaporation, the fluid molecules with CN = 2, 3 and 4 are marked and observed by OVITO software (see Fig. 4) [32]. In the vapor region, fluid molecules are observed with CN = 2 and 3 but are rarely or never observed with CN = 4. Therefore, the molecules with CN = 4 are identified as interface molecules. Correspondingly according to the definition of CN, the interface density is obtained: $\rho = 5/(4/3 \cdot \pi \cdot (1.5\sigma_{ff})^3)$ Å^{-3}. Note that it should include the center molecule when calculating density, so the numerator is 5.

Figure 5 shows the evolution of evaporation meniscus for $P48D16H36$ at (a) $\Delta T = 10$ K and (b) $\Delta T = 35$ K. Note that two z axes are the position of the nanopillar surface ($x = \pm 62.72$ Å). Initially, the liquid-vapor interface moves upward due to thermal expansion. This is less apparent when ΔT is smaller. Then the curvature of the interface near the nanopillar surface increases gradually during evaporation, correspondingly the contact angle decreases. In our simulations, because a strong fluid-solid bonding strength parameter is used (i.e., perfectly wetting fluid is simulated), the interface is still pinned at the top of the nanopillars even when the nanofilm approaches the substrate surface. Additionally, it is also seen that the curvature of meniscus close to the nanopillars changes dramatically while the meniscus is almost flat in the centre region. This is more apparent for larger ΔT.
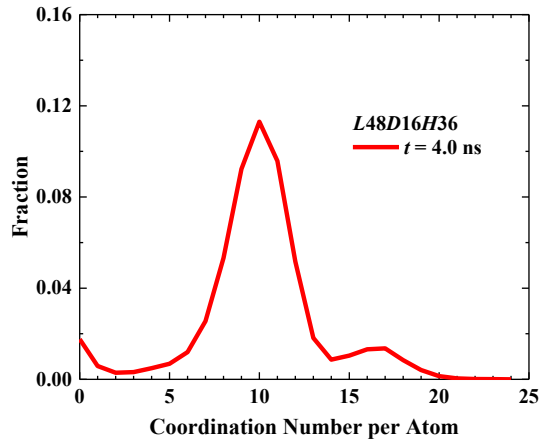

9

Fig. 3 The normalized histogram of the coordination number per fluid molecule for *P*48*D*16*H*36 when *t* = 4.0 ns.
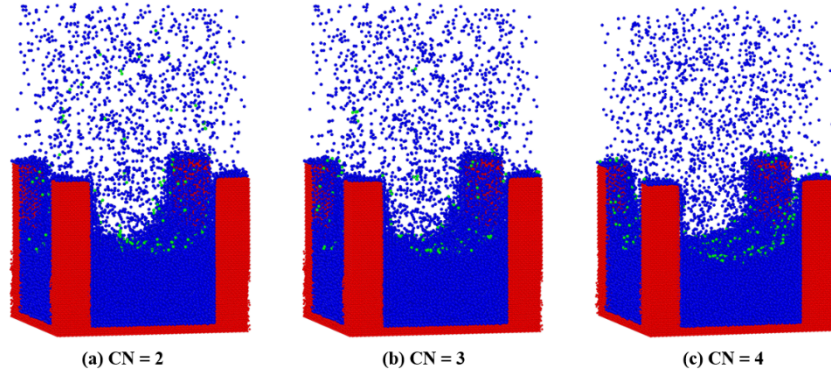

(a) CN = 2   (b) CN = 3   (c) CN = 4

Fig. 4 Atoms with different coordination number (CN) are marked in green in the snapshot for *L*48*D*16*H*36 when *t* = 4.0 ns. (a)CN = 2; (b)CN = 3; (c) CN=4.
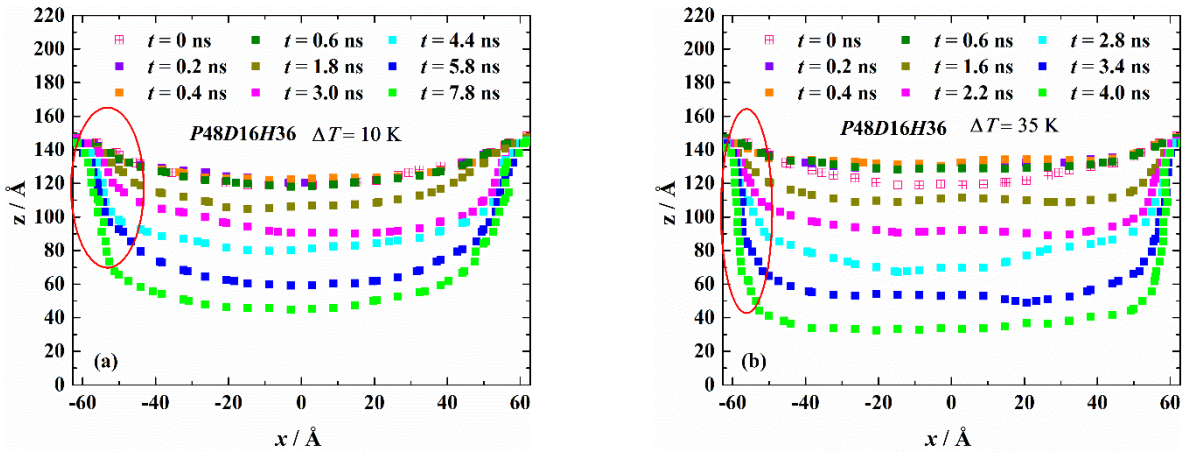

Fig. 5 Evaporation meniscus (liquid-vapor interface) shapes for *P*48*D*16*H*36 at (a) Δ*T* = 10 K and (b) Δ*T* = 35 K

Onset and Evolution of Nanobubbles

In some applications, pure evaporation in the absence of boiling is preferred due to its stable nature compared with the chaotic boiling process and the boiling limit. Thus, locating the onset of boiling is necessary. We increase Δ*T* to 40 K and try observing the onset and evolution of nanobubbles under *P*48*D*16*H*36 case. Figure 6 shows the density contour of fluid at different time. To clearly monitor the onset and evolution of nanobubbles, the fluid density below 0.009 Å^{-3} (the liquid-vapor interface density and see the Dynamics of Evaporation Meniscus section) is cut-off. As can be seen in Fig. 6, nanobubbles first appears around the bottom of

nanopillars. Then bubbles in the corner coalescence and expand towards the center of the cell. Due to strong solid-fluid wettability, nanobubbles do not originate from the solid surface and there is a non-evaporation ultrathin film covering in the solid surface, which is also observed in other studies [33][34]. To further understand this, the potential energy contour of fluid is calculated (see Fig. 7). From energy point of view [35][36], low potential energy means large energy barrier for evaporation or boiling and only when liquid overcomes their potential barrier can the bubble nucleus form. As can be seen in Fig. 7, fluid close to the solid surface owes much low potential energy, which strongly impedes the evaporation and boiling. This is why nanobubbles do not originate from the solid surface. Before the fluid is heated ($t = 0$ ns), the potential energy of fluid uniformly distributes in the bulk region. Once the solid temperature is increased, fluid absorbs thermal energy from the heating solid, and some of the thermal energy is converted to the potential energy, which leads to the increase in potential energy of fluid. The potential energy of fluid close to the solid surface first increases, then this increase propagates towards the center (see $t = 0.2$ ns and $t = 0.4$ ns). It can also be found that the potential energy of fluid around the nanopillars corner increases more quickly, which eventually leads to nanobubbles first appearing there when they overcome the energy barrier. The reason is because the fluid around the nanopillars corner can absorb more thermal energy not only from substrate but also from nanopillars compared with fluid in other regions. In summary, nanobubbles appear when fluid overcomes its potential energy barrier, and they prefer to appear around nanopillars corner as the potential energy of fluid increases the most quickly there.
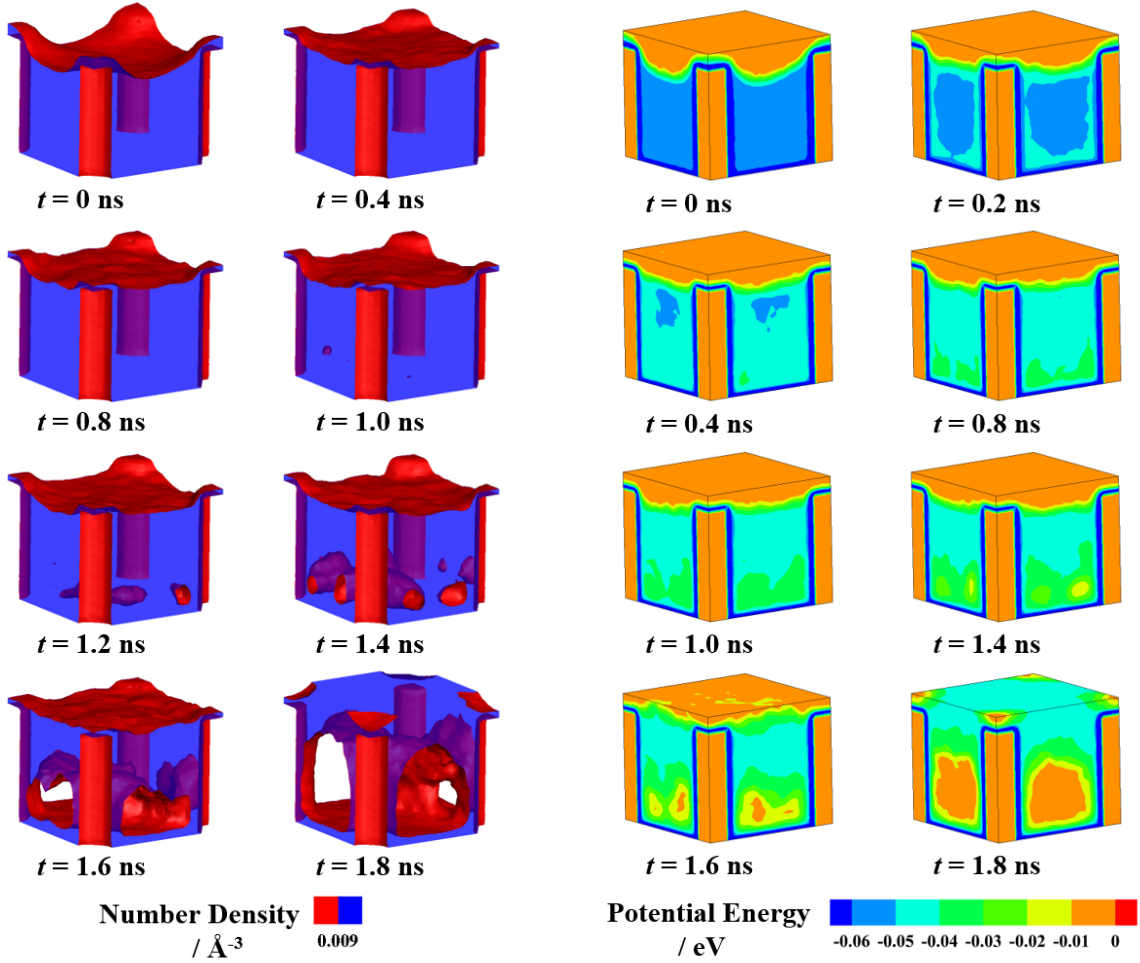
Fig. 6 Snapshots of fluid density contour for *P*48*D*16*H*36 at Δ*T* = 40 K. Density below 0.009 Å^{-3} is cut-off.

Fig. 7 Snapshots of potential energy contour of fluid for *P*48*D*16*H*36 at Δ*T* = 40 K.

Nanostructure Design for Stable and Efficient Pure Evaporation

The effect of structure geometry on evaporation and boiling is systematically investigated in the present study. This helps tailor performance of wick-based evaporators. As mentioned before, to achieve stable heat transfer, evaporation without boiling is preferred. Figures 8 to 10 present the fluid density contour and potential energy contour under different cases. By varying *P*, *D* and *H*, respectively (see Sec. 2 in supporting information), we found that for fixed Δ*T*, decreasing *P* (see Fig. 8) and increasing *D* (see Fig. 9) and *H* (see Fig. 10), individually, raise the possibility of boiling. From the potential energy contour, we found that after decreasing *P*

(see Fig. 8) and increasing D (see Fig. 9) and H (see Fig. 10), individually, the increase in the potential energy of fluid around nanopillars corner becomes faster and the energy is easily accumulated to overcome the energy barrier of forming nanobubble. Thus, nanobubbles appears in those cases.

Figures 11 to 13 plot evaporation mass flux ($\dot{m}''$) as a function of nanofilm thickness (δ) on nanopillar surfaces with different geometrical parameters and that on smooth surface. To obtain $\dot{m}''$, the coordination number and position data of each fluid molecule are collected every 4×10^4 time steps. Molecules with CN $\geq$ 4 are identified as fluid molecules (see the Dynamics of Evaporation Meniscus section). $\dot{m}''$ is calculated as the time rate of change of the number of liquid molecules in the unit cell using a central difference formula. Note that the evaporation area to calculate $\dot{m}''$ is adopted $P\times P$, the total cross area of the simulated unit cell. As can be seen in these figures, generally, $\dot{m}''$ increases as decreasing P and H and increasing D; $\dot{m}''$ first increases with the decrease in δ, which results from the decrease in the conduction thermal resistance of liquid with δ decreasing. But with P decreasing or D increasing, heating area increases so there quickly behaves steady $\dot{m}''$ (e.g., $P48D16H36$ in Fig. 11 and $P64H36D32$ in Fig. 12). Additionally, there exists the saturation of the increase in $\dot{m}''$ when increasing D ($D24$ and $D32$ in Fig. 12). Combining the results about the effect of structure geometry on boiling, we need trade-offs to decide D, L and H when designing a wick-based evaporator for stable pure evaporation.

When the film thickness decreases to a threshold, $\dot{m}''$ for all cases starts dropping dramatically. According to previous research [37]-[39], it means that disjoining pressure ($P_d = B/\delta^3$, where B is the dispersion constant) starts showing effect, and it increases with decreasing δ. P_d was proposed for treating the effect of the solid-fluid force interaction in thin liquid film and it shows a strong suppression effect on evaporation. In our simulations, the film thickness where

P_d starts showing effect is the same for both smooth and nanopillar surfaces and it is around 20 Å. To maintain efficient evaporation, δ should be forced larger than this threshold. Additionally, there also shows that the $\dot{m}''$ of the smooth surface surpasses those of nanopillar surfaces when δ is smaller than a certain value (indicated by grey arrows). This is because although adopting nanopillars in a smooth surface enhances evaporation due to the increase in heating area, the evaporation flux simultaneously is suppressed due to the decrease in the volume of supplied fluid and the existence of capillary pressure [39]. As δ decreases, the suppression effects on $\dot{m}''$ is gradually more significant than the enhancement effect. Thus, to enhance pure evaporation on nanopillar surface compared with that on smooth surface, the nanofilm thickness should be maintained beyond the value where the suppression effects on $\dot{m}''$ due to the decrease in the volume of supplied liquid and the existence of capillary pressure dominates during evaporation. This also explains that why in Fig. 12, for fixed P and H, when D increases to $24a$, the increase in $\dot{m}''$ saturates.
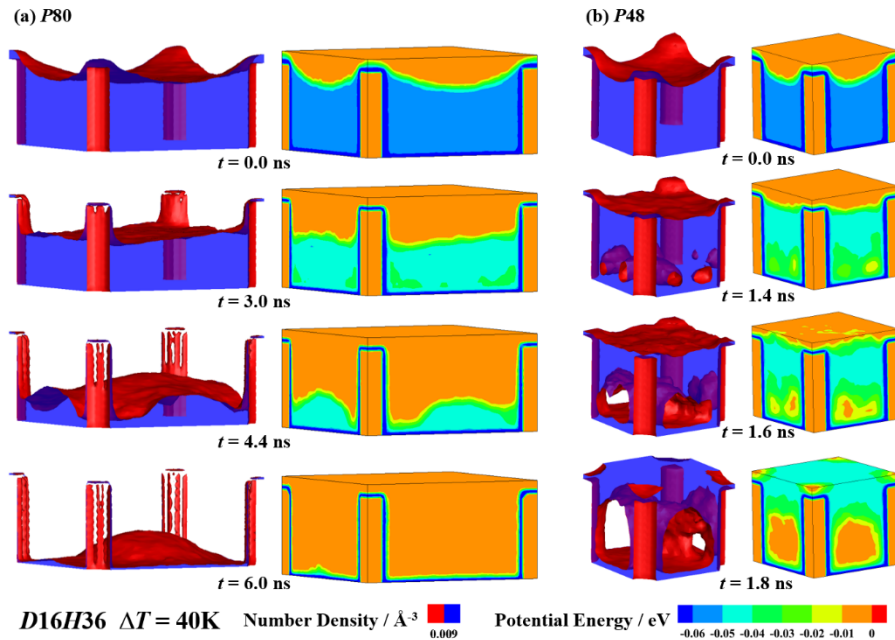

Fig. 8 Snapshots of fluid density contour and potential energy contour for $D16H36$ with different pitch between nanopillars at $\Delta T = 40K$ (a) $P80$; (b) $P48$. Density below 0.009 Å^{-3} is cut-off.
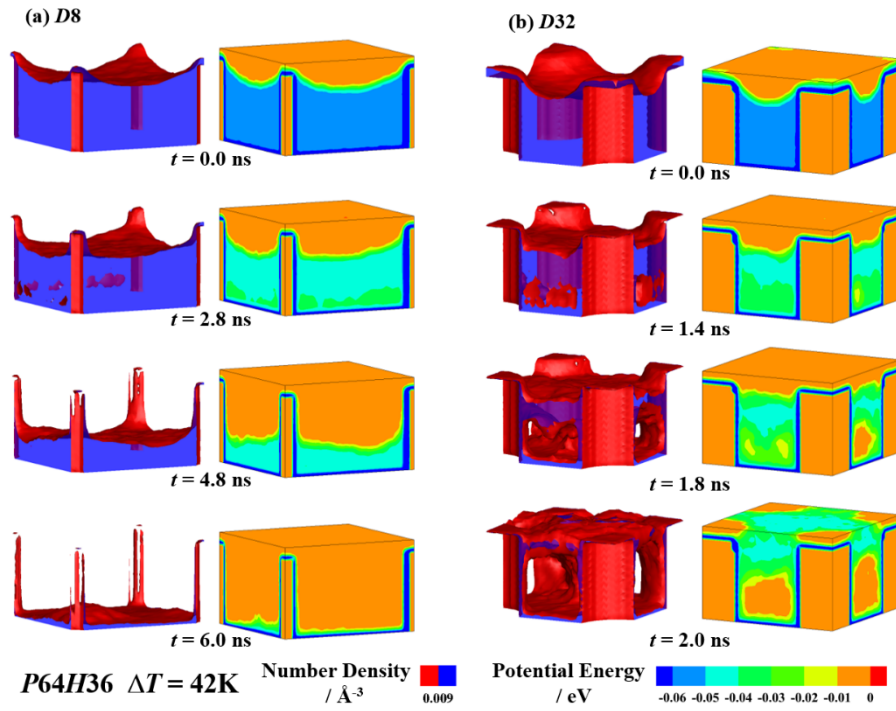
Fig. 9 Snapshots of fluid density contour and potential energy contour for *P*64*H*36 with different diameter of nanopillars at Δ*T* = 42K (a) *D*8; (b) *D*32. Density below 0.009 Å^{-3} is cut-off.
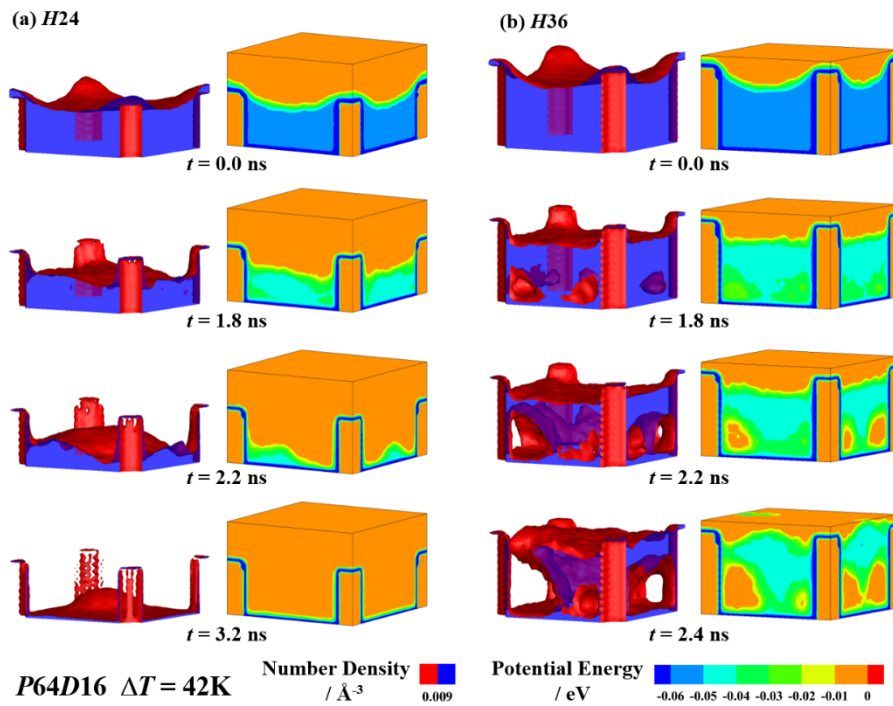
Fig. 10 Snapshots of fluid density contour and potential energy contour for $P64D16$ with different height of nanopillars at $\Delta T = 42K$ (a) $H24$; (b) $H36$. Density below 0.009 Å^{-3} is cut-off.
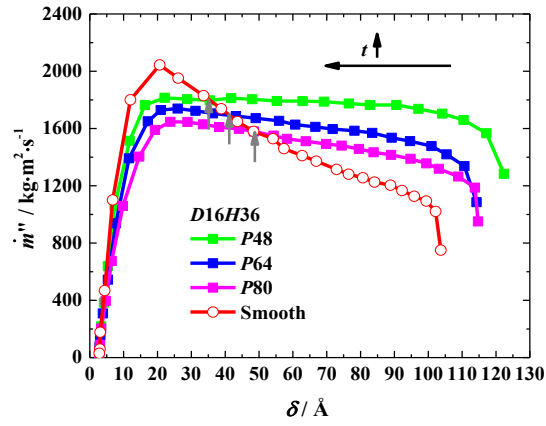

Fig. 11 Evaporation mass flux ($\dot{m}''$) vs nanofilm thickness (δ) for fixed D and H cases. δ decreases as t

(evaporation time) increases.
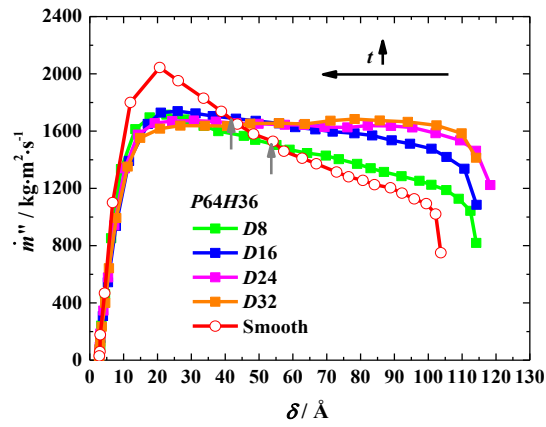
Fig. 12 Evaporation mass flux ($\dot{m}''$) vs nanofilm thickness (δ) for fixed P and H cases. δ decreases as t

(evaporation time) increases.

16
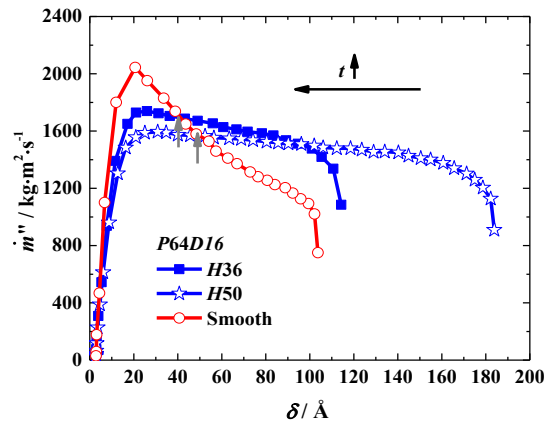
Fig. 13 Evaporation mass flux ($\dot{m}''$) vs nanofilm thickness (δ) for fixed P and D cases. δ decreases as t (evaporation time) increases.

CONCLUSIONS

In this work, characteristics of evaporation and how to maintain and enhance nanofilm evaporation without boiling on nanopillar surface were investigated using MD method.

For the perfectly wetting fluid, the meniscus can be still pinned at the top of the nanopillars even when the nanofilm is quite close to the surface of substrate and the curvature of the meniscus near nanopillars varies dramatically during evaporation. On nanopillar surface, nanobubbles prefer to first develop around nanopillars corner due to the quick increase in the potential energy of fluid there, then coalesce and expand toward the unit center.

Based on our parametric study, the evaporation mass flux $\dot{m}''$ can be increased by decreasing P and increasing D but these also raise the risk of boiling. However, decreasing H can both benefit evaporation and suppress boiling. Therefore, we should have a trade-off between enhancing evaporation and achieving stable evaporation without boiling when selecting P, D and H.

During evaporation, to maintain efficient evaporation and avoid the suppression effect of disjoining pressure on evaporation, nanofilm thickness should be forced beyond a threshold where disjoining pressure starts showing effect. In this work, the threshold value is about 20 Å. To enhance the evaporation on nanopillar surface against smooth surface, the film thickness should be maintained larger than the value where the suppression effect on evaporation due to the decrease in the volume of supplied fluid and the existence of capillary pressure behaves more significant than the enhancement effect on evaporation due to the increase in the heating area.

ASSOCIATED CONTENT

Supporting Information

Equilibrium MD simulation for fluid properties; the effect of structure geometry for the type of heat transfer. (PDF)

AUTHOR INFORMATION

Corresponding Author

*E-mail: sunjie@xjtu.edu.cn (JS).

Notes

The authors declare no competing financial interest.
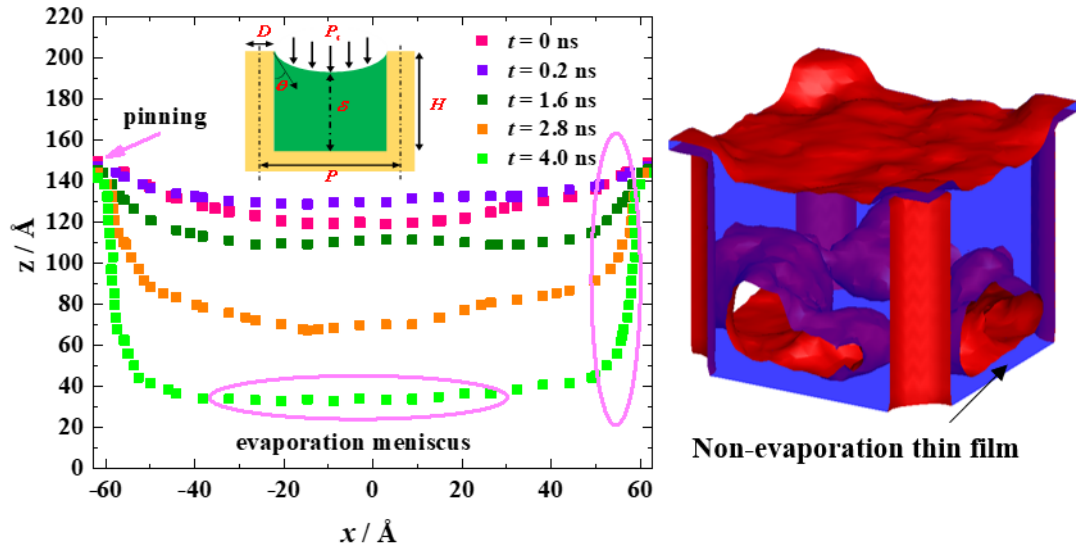
ACKNOWLEDGEMENTS

REFERENCES

[1] Plawsky, J. L.; Fedorov, A. G.; Garimella, S. V.; Ma, H. B.; Maroo, S. C.; Chen, L.; Nam, Y., Nano- and Microstructures for Thin-Film Evaporation—A Review. *Nanosc. Microsc. Therm.* **2014**, 18, 251-269.

[2] Edalatpour, M.; Liu, L.; Jacobi, A. M.; Eid, K. F.; Sommers, A. D., Managing water on heat transfer surfaces: A critical review of techniques to modify surface wettability for applications with condensation or evaporation. *Appl. Energy* **2018**, 222, 967-992.

[3] Zhu, L.; Gao, M.; Peh, C. K. N.; Ho, G. W., Recent progress in solar-driven interfacial water evaporation: Advanced designs and applications. *Nano Energy* **2019**, 57, 507-518.

[4]Pang, Y.; Zhang, J.; Ma, R.; Qu, Z.; Lee, E.; Luo, T., Solar−Thermal Water Evaporation: A Review. *ACS Energy Lett.* **2020**, 5, 437-456.

[5] Pu, J. H.; Sun, J.; Wang, W.; Wang, H. S., Generation and Evolution of Nanobubbles on Heated Nanoparticles: A Molecular Dynamics Study. *Langmuir* **2020**, 36, 2375-2382.

[6] Vaartstra, G.; Zhang, L.; Lu, Z.; Díaz-Marín, C. D.; Grossman, J. C.; Wang, E. N., Capillary-fed, thin film evaporation devices. *J. Appl. Phys.* **2020**, 128, 130901.

[7] Cao, Q.; Cui, Z.; Shao, W., Optimization Method for Grooved Surface Structures Regarding the Evaporation Heat Transfer of Ultrathin Liquid Films at the Nanoscale. *Langmuir* **2020**, 36, 2802-2815.

[8] Li, C.; Lan, C.; Guo, M.; Wang, N.; Ma, Y., Wicking-Driven Evaporation Self-Assembly of Carbon Nanotubes on Fabrics: Generating Controlled Orientational Structures. *Langmuir* **2020**, 36, 13963-13970.

[9] Li, R.; Wang, J.; Xia, G., New Model for Liquid Evaporation and Vapor Transport in Nanopores Covering the Entire Knudsen Regime and Arbitrary Pore Length. *Langmuir* **2021**, 37, 2227-2235.

[10] Somasundaram, S.; Zhu, Y.; Lu, Z.; Adera, S.; Bin, H.; Mengyao, W.; Tan, C. S.; Wang, E. N., Thermal design optimization of evaporator micropillar wicks. *Int. J. Therm. Sci.* **2018**, 134, 179-187.

[11] Tang, H.; Tang, Y.; Wan, Z.; Li, J.; Yuan, W.; Lu, L.; Li, Y.; Tang, K., Review of applications and developments of ultra-thin micro heat pipes for electronic cooling. *Appl. Energy* **2018**, 223, 383-400.

[12] Zhou, X.; Zhao, F.; Guo, Y.; Zhang, Y.; Yu, G., A hydrogel-based antifouling solar evaporator for highly efficient water desalination. *Energy Environ. Sci.* **2018**, 11, 1985-1992.

[13] Ranjan, R.; Patel, A.; Garimella, S. V.; Murthy, J. Y., Wicking and thermal characteristics of micropillared structures for use in passive heat spreaders. *Int. J. Heat Mass Tran.* **2012**, 55, 586-596.

[14] Ravi, S.; Horner, D.; Moghaddam, S., Monoporous micropillar wick structures, I-Mass transport characteristics. *Appl. Therm. Eng.* **2014**, 73, 1371-1377.

[15] Horner, D.; Ravi, S.; Moghaddam, S., Monoporous micropillar wick structures, II-optimization & theoretical limits. *Appl. Therm. Eng.* **2014**, 73, 1378-1386.

[16] Adera, S.; Antao, D.; Raj, R.; Wang, E. N., Design of micropillar wicks for thin-film evaporation. *Int. J. Heat Mass Tran.* **2016**, 101, 280-294.

[17] Farokhnia, N.; Irajizad, P.; Sajadi, S. M.; Ghasemi, H., Rational Micro/Nanostructuring for Thin-Film Evaporation. *J. Phys. Chem. C* **2016**, 120, 8742-8750.

[18] Ravi, S.; Dharmarajan, R.; Moghaddam, S., Physics of Fluid Transport in Hybrid Biporous Capillary Wicking Microstructures. *Langmuir* **2016**, 32, 8289-8297.

[19] Zhu, Y.; Antao, D. S.; Lu, Z.; Somasundaram, S.; Zhang, T.; Wang, E. N., Prediction and Characterization of Dry-out Heat Flux in Micropillar Wick Structures. *Langmuir* **2016**, 32, 1920-1927.

[20] Antao, D. S.; Adera, S.; Zhu, Y.; Farias, E.; Raj, R.; Wang, E. N., Dynamic Evolution of the Evaporating Liquid-Vapor Interface in Micropillar Arrays. *Langmuir* **2016**, 32, 519-526.

[21] Lu, Z.; Preston, D. J.; Antao, D. S.; Zhu, Y.; Wang, E. N., Coexistence of Pinning and Moving on a Contact Line. *Langmuir* **2017**, 33, 8970-8975.

[22] Cho, S.; Tummala, R.; Joshi, Y., Capillary Performance of Micropillar Arrays in Different Arrangements. *Nanosc. Microsc. Therm.* **2018**, 22, 97-113.

[23] Wei, M.; He, B.; Liang, Q.; Somasundaram, S.; Tan, C. S.; Wang, E. N., Optimization and thermal characterization of uniform silicon micropillar based evaporators. *Int. J. Heat Mass Tran.* **2018**, 127, 51-60.

[24] Zhang, L.; Zhu, Y.; Lu, Z.; Zhao, L.; Bagnall, K. R.; Rao, S. R.; Wang, E. N., Characterization of thin film evaporation in micropillar wicks using micro-Raman spectroscopy. *Appl. Phys. Lett.* **2018**, 113, 163701.

[25] Wang, R.; Jakhar, K.; Antao, D. S., Unified Modeling Framework for Thin-Film Evaporation from Micropillar Arrays Capturing Local Interfacial Effects. *Langmuir* **2019**, 35, 12927-12935.

[26] Cai, Q.; Bhunia, A., High heat flux phase change on porous carbon nanotube structures. *Int. J. Heat Mass Tran.* **2012**, 55, 5544-5551.

[27] Ćoso, D.; Srinivasan, V.; Lu, M.-C.; Chang, J.-Y.; Majumdar, A., Enhanced Heat Transfer in Biporous Wicks in the Thin Liquid Film Evaporation and Boiling Regimes. *J. Heat Transfer* **2012**, 134, 101501.

[28] Cai, S. Q.; Bhunia, A., Characterization of Phase Change Heat and Mass Transfers in Monoporous Silicon Wick Structures. *J. Heat Transfer* **2014**, 136, 072001.

[29] Plimpton S. Fast parallel algorithms for short-range molecular dynamics[J]. *J. Comput. Phys.* **1995**, 117: 1-19.

[30] Pu, J. H.; Sun, J.; Sheng, Q.; Wang, W.; Wang, H. S., Dependences of Formation and Transition of the Surface Condensation Mode on Wettability and Temperature Difference. *Langmuir* **2020**, 36, 456-464.

[31] Tang, G.; Niu, D.; Guo, L.; Xu, J., Failure and Recovery of Droplet Nucleation and Growth on Damaged Nanostructures: A Molecular Dynamics Study. *Langmuir* **2020**, 36, 13716-13724.

[32] Stukowski, A., Visualization and analysis of atomistic simulation data with OVITO–the Open Visualization Tool. *Model. Simul. Mater. Sci. Eng.* **2009**, 18, 015012.

[33] Akkus, Y.; Koklu, A.; Beskok, A., Atomic Scale Interfacial Transport at an Extended Evaporating Meniscus. *Langmuir* **2019**, 35, 4491-4497.

[34] Chen, Y.; Li, J.; Yu, B.; Sun, D.; Zou, Y.; Han, D., Nanoscale Study of Bubble Nucleation on a Cavity Substrate Using Molecular Dynamics Simulation. *Langmuir* **2018**, 34, 14234-14248.

[35] Chen, Y. J.; Chen, X. J.; Yu, B.; Zou, Y.; Tao, W. Q., Molecular Dynamics Study of Bubble Nucleation on an Ideally Smooth Substrate. *Langmuir* **2020**, 36, 13725-13734.

[36] Chen, Y.-J.; Yu, B.; Zou, Y.; Chen, B.-N.; Tao, W.-Q., Molecular dynamics studies of bubble nucleation on a grooved substrate. *Int. J. Heat Mass Tran.* **2020**, 158, 119850.

[37] Yu, J.; Wang, H., A molecular dynamics investigation on evaporation of thin liquid films. *Int. J. Heat Mass Tran.* **2012**, 55, 1218-1225.

[38] Wang, X.; Li, Y.; Malen, J. A.; McGaughey, A. J. H., Assessing the impact of disjoining pressure on thin-film evaporation with atomistic simulation and kinetic theory. *Appl. Phys. Lett.* **2020**, 116, 213701.

[39] Wang, H.; Garimella, S. V.; Murthy, J. Y., Characteristics of an evaporating thin film in a microchannel. *Int. J. Heat Mass Tran.* **2007**, 50, 3933-3942.

For Table of Contents Only